

Article

# Numerical Analysis of Combined Wave Radiation and Diffraction on a Floating Barge

Yajie Li <sup>1</sup> , Bin Xu <sup>1,\*</sup> , Desheng Zhang <sup>1</sup>, Xi Shen <sup>1</sup> and Weibin Zhang <sup>2</sup>

<sup>1</sup> Research Center of Fluid Machinery Engineering and Technology, Jiangsu University, Zhen Jiang 212013, China; yajieli@ujs.edu.cn (Y.L.); zds@ujs.edu.cn (D.Z.); shen.xi.01@outlook.com (X.S.)

<sup>2</sup> Key Laboratory (Fluid Machinery and Engineering Research Base) of Sichuan Province, Xihua University, Sichuan 610039, China; zhangwb@mail.xhu.edu.cn

\* Correspondence: norkistar@ujs.edu.cn

Received: 21 October 2019; Accepted: 7 January 2020; Published: 11 January 2020



**Abstract:** A two-dimensional boundary element method (BEM) based on the potential flow theory is adopted to study the combined wave radiation and diffraction by a single barge. The wave-body interaction problems are simulated using a mixed Euler-Lagrangian scheme, with fully nonlinear boundary conditions. The numerical schemes are verified through comparing with existing results, which show that both the wave runups on the barge and hydrodynamic forces can be calculated with sufficient accuracy. Cases of a single barge subjected to sway motion and regular waves are studied. The real contribution of this study is the outcomes of the spectral analysis conducted for test cases when wave radiation effects are considered in addition to pure wave diffraction. The cases of sway motion with the same frequency as incident wave are simulated first. It is found that sway motion will reduce the overall horizontal force when the frequency is lower than a critical frequency. After that, the higher the frequency, the bigger the horizontal force increasing effect. When the frequency of sway motion is lower than that of incident wave, in terms of the magnitude of the horizontal force, sway motion of the body will always make the resultant force larger than that of pure diffraction case.

**Keywords:** wave–structure interaction; boundary element method; potential flow theory; numerical wave tank

## 1. Introduction

The hydrodynamic interactions between water waves and floating bodies have long been studied in fluid dynamics. Within the context of velocity potential flow theory, there are generally two categories of methods available to treat the wave–body interaction problems. One group is the frequency domain solution, which is mainly based on the Stokes wave theory for periodic motion, without considering the initial transient effect; the other is the time domain solution to the resulting wave field and hydrodynamic performance of the body. During the last three decades, the time domain method has gained its popularity gradually in parallel with the development of high-performance computers. The most widely used time domain method is based on the mixed Eulerian-Lagrangian time stepping approach proposed by Longuet-Higgins and Cokelet [1]. By this method, the flow field equations in the Eulerian description are solved at every time step, and the exact free surface position and the velocity potential of the next time step can be updated in the Lagrangian framework.

Wave radiation problem is related to a rigid body in forced motions in otherwise calm water, which can generate outgoing waves. The oscillating fluid pressure resulting from the fluid motions and radiated waves is the source of hydrodynamic forces. The study of wave radiation problem dated at least back to Ursell [2]. He studied the harmonic heave motion of a horizontal circular cylinder in infinite water depth. The very long cylinder assumption caused the problem to be reduced

to two-dimensional (2D). Kim [3] proposed a solution of the potential problem associated with the harmonic oscillation of an ellipse (2D) or ellipsoid (3D). The hydrodynamic coefficients of all six motion modes were provided. Black et al. [4] calculated the radiation problem including heave, sway, and roll of a rectangular section (2D) and a vertical circular cylinder (3D) by employing Schwinger's variational formulation. An analytical solution to the heave radiation of a rectangular body was presented by Lee [5], who divided the whole fluid region into three sub-regions and solved the non-homogeneous boundary value problem analytically. All the above-mentioned studies are based on the linear theory. Later, fully nonlinear potential flow theory in the time domain dominated the study of radiation problem. Wu and Eatock Taylor [6] considered a 2D submerged circular cylinder subjected to forced sway or heave motion. Domain decomposition technique was also used in this paper to satisfy the radiation condition on the truncated boundary. Maiti and Sen [7] presented and discussed the heave radiation forces for both rectangular and triangular hull. A 3D vertical cylinder that underwent periodic oscillation in the open sea and in a channel were studied by Hu et al. [8] using the finite element method. Wang et al. [9] considered a flared spar subjected to forced sway or heave motions, with three different amplitudes, in an open sea.

The wave diffraction problem is related to a fixed body under incident waves. For a vertical cylinder extending down to an infinite water depth subjected to plane waves, it was first solved analytically by Havelock [10] using linearized free surface boundary conditions, and only linear hydrodynamic force was calculated. With the development of offshore floating platforms, some phenomenon associated with mean drift forces, sum, or difference frequency forces became important, which cannot be explained by linear diffraction theory. Second-order diffraction theory [11–14] was then established, in which the free surface was taken as its mean position as in the linear theory, but all the terms in free surface boundary conditions as well as the expansion for the instantaneous position, fluid pressure, and wave loads were kept to the order of square of the wave amplitude or wave steepness. For many offshore structures like tension leg platforms, which are, in general, designed to have high natural frequencies, ringing and spring are commonly observed. Studies show that they are most likely to be excited by force at high frequencies and typically third-order forces at triple wave frequency. Hence, third-order diffraction theory [15–17] was developed. It should be pointed out that third-order diffraction theory involved lengthy equations and it was seldom used in practical problems for a real platform. The most common approach, instead of extending the diffraction theory to higher-order, was developing fully nonlinear theory. Numerical simulations were adopted in the fully nonlinear theory in the time domain. All high-order components of wave forces can be attained through Fourier analysis of the force history. Ma et al. [18] studied three-dimensional bottom-mounted circular cylinder under monochromatic and irregular waves numerically using fully nonlinear potential flow theory. Bai and Eatock Taylor [19] did fully nonlinear numerical simulation of vertical cylinder under regular and focused wave. Domain decomposition technique was implemented to increase the efficiency of the calculation. Wang et al. [9] simulated a spar platform with three different angles, in a numerical tank under regular and irregular incident waves. Wave diffraction by an axisymmetric flared body formed from a parabolic generating curve was studied by Bai and Eatock Taylor [20].

Wave radiation and diffraction problem is related to a floating body under incident waves. The study is to predict wave loads and motion responses of the body. Strip theory and slender body theory are both classic linear theories in early days, depending on the characteristics of incident waves and the feature of body geometries. For practical problems involving large body motions, and/or incident waves, the significance of nonlinear effects should be accounted for. Second-order theory, associated with second-order hydrodynamic forces and mean drift forces, needs to be developed and used. The main difficulty is to obtain second-order velocity potential, even computationally. A review of second-order theory was given by Ogilvie [21]. Then, fully nonlinear wave theory was required when all levels of nonlinear effects need to be captured. That is when the incident waves and the resulting body motions are large or even violent. The fully nonlinear wave interactions with freely floating body require special treatment of the nonlinear coupling between hydrodynamic force and

the body motion. Much research has been carried out for simplified 2D problem. Cao et al. [22] studied a free floating rectangular box in incident waves generated by a pneumatic wave maker. Sway, heave, and roll modes were all considered. Kashiwagi [23] investigated incident wave-induced motions of a wall-sided body (resembling mid-ship section) and a flared floating body (resembling ship bow section) by numerical simulation and model tests. Koo and Kim [24] simulated a freely floating barge in a numerical tank. Yan and Ma [25] used a finite element method to study a freely floating barge moored to the walls of a numerical tank. In the present work, the combined wave radiation and diffraction problems will be studied based on the fully nonlinear potential flow theory in the time domain other than pure radiation and diffraction problems. Specifically, the effects of sway motion on wave diffraction will be analyzed because in such a case, the wave interactions can be strengthened when the body is moving towards the incoming wave or weakened when it is moving away. The results are compared with that of pure diffraction cases. The paper is organized as below. In Section 2, we outline the mathematical formulation and numerical procedure of the present problem. In Section 3, the validation and numerical results and discussions are provided for the barge in pure diffraction by steep incident waves, and in combined radiation and diffraction. Both the cases of the sway motion with the same and different frequencies from incident wave are simulated. The spectral analysis is conducted for the simulated cases to uncover some interesting findings. Conclusions are provided in Section 4.

## 2. Mathematical Model and Numerical Procedure

The wave-body interaction problem is studied through the fully nonlinear velocity potential theory. This implies that the fluid itself is inviscid, incompressible, and the fluid velocity field is irrotational.

### 2.1. Mathematical Model and Formulations

The physical problem of wave interactions with a floating body is shown in Figure 1. The body of rectangular shape has width  $B$  and initial draught  $D$ . The right-handed Cartesian coordinate system is employed with  $z$ -axis directing vertically upwards and  $x$ -axis lying in the still water surface from left to right. The water depth is denoted as  $h$ . Two artificial ‘walls’ are placed at some distance away from the body to make the fluid domain finite in the computation. The governing equation and the boundary conditions are presented below.

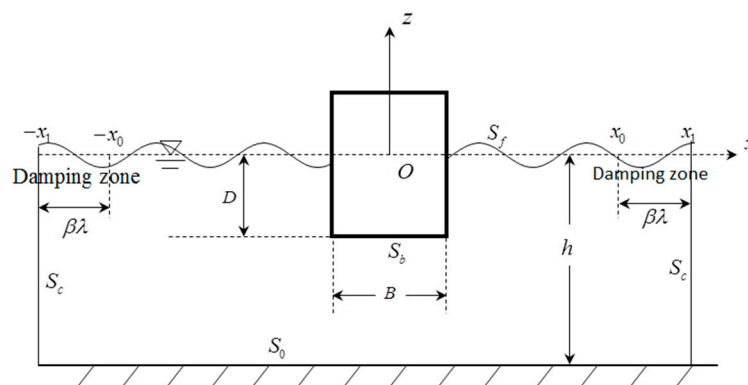


Figure 1. Sketch of the water waves interaction with a single barge.

The flow in the fluid domain is governed by Laplace’s equation:

$$\nabla^2 \phi = 0. \tag{1}$$

$\phi$  denotes the velocity potential. On the free surface, there exist both kinematic and dynamic conditions. They can be expressed as shown in Equation (2);  $g$  denotes gravitational acceleration and  $\eta$  is the free surface elevation.

$$\frac{\partial \eta}{\partial t} + \frac{\partial \phi}{\partial x} \frac{\partial \eta}{\partial x} - \frac{\partial \phi}{\partial z} = 0, \quad \frac{\partial \phi}{\partial t} + \frac{1}{2} |\nabla \phi|^2 + g\eta = 0. \tag{2}$$

On the wetted body surface and sea bottom, the impermeability condition should be satisfied. The truncated boundaries are fixed rigid walls. To minimize the reflection by the artificial walls, a damping layer located in front of each truncated boundary is applied on the free surface. Ideally, the outgoing waves can be damped out completely by the artificial damping sponge. Thus, ‘non-reflecting boundary conditions’ can be adopted in the numerical solutions of wave problems. Therefore, we have

$$\partial \phi / \partial n = \partial \phi_I / \partial n \tag{3}$$

with incoming waves denoted by  $\phi_I$ .

The total velocity potential and free surface elevation can be decomposed into two parts:

$$\phi = \phi_I + \phi_D, \quad \eta = \eta_I + \eta_D, \tag{4}$$

where  $\eta_I$  describes the free surface elevation induced by incident waves.  $\phi_D$  and  $\eta_D$  denote the disturbed velocity potential and free surface elevation, respectively. This decomposition enables us to solve the disturbed velocity potential instead of the total velocity potential.

Substituting Equation (4) into the governing equation and boundary conditions, we can obtain the corresponding equations for  $\phi_D$  as following [26,27]:

$$\left\{ \begin{array}{ll} \nabla^2 \phi_D = 0, & \text{in the fluid domain} \\ \frac{\partial \phi_D}{\partial t} = \frac{\partial \phi}{\partial t} - \frac{\partial \phi_I}{\partial t} = -\frac{1}{2} |\nabla \phi_I + \nabla \phi_D|^2 - g\eta - \frac{\partial \phi_I}{\partial t} & \text{on } S_f, \\ \frac{\partial \phi_D}{\partial n} = \frac{\partial \phi}{\partial n} - \frac{\partial \phi_I}{\partial n} = (\vec{U} - \nabla \phi_I) \cdot \vec{n} & \text{on } S_b, \\ \frac{\partial \phi_D}{\partial n} = \frac{\partial \phi}{\partial n} - \frac{\partial \phi_I}{\partial n} = -\nabla \phi_I \cdot \vec{n} & \text{on } S_0, \\ \frac{\partial \phi_D}{\partial n} = \frac{\partial \phi}{\partial n} - \frac{\partial \phi_I}{\partial n} = 0 & \text{on } S_c. \end{array} \right. \tag{5}$$

$\vec{n}$  is the unit normal vector along the body surface and  $\vec{U}$  represents the translational velocities of body. Rotational motion of the body is restrained. For the initial condition on the free surface, we have

$$\eta_D = 0, \quad \phi_D = 0 \quad \text{at } t = 0. \tag{6}$$

Equations (5) and (6) completely define the initial boundary value problem (IBVP) for the disturbed flow.

### 2.1.1. Time Stepping Approach

In the time domain study, solving the initial boundary value problem in the above Eulerian framework gives us the velocity potential at a given time. Lagrangian specification should then be employed to track the flow quantities from time to time. The kinematic and dynamic boundary conditions on the free surface can be expressed in their Lagrangian form as:

$$\frac{Dx}{Dt} = \frac{\partial \phi}{\partial x}, \quad \frac{Dz}{Dt} = \frac{\partial \phi}{\partial z}, \quad \frac{D\phi}{Dt} = \frac{1}{2} |\nabla \phi|^2 - g\eta, \tag{7}$$

where  $D/Dt = \partial/\partial t + \nabla \phi \cdot \nabla$  is the material derivative following a given fluid particle. We are able to follow the free surface elevation and velocity potential from one position on the free surface to the

succeeding position using Equation (7). Numerically, the updating of the free surface and velocity potential can be realized by integration of the total differentials with small time steps.

It has been mentioned that to satisfy the radiation condition, an artificial damping zone is added to minimize the reflection of the truncated boundaries. This is achieved by adding a damping term in Equation (7) artificially. Therefore, they become

$$\frac{Dx}{Dt} = \frac{\partial\phi}{\partial x}, \quad \frac{Dz}{Dt} = \frac{\partial\phi}{\partial z} - v(x)z, \quad \frac{D\phi}{Dt} = \frac{1}{2}|\nabla\phi|^2 - g\eta - v(x)\phi, \tag{8}$$

in which  $v(x)$  is the damping coefficient, as expressed in Cointe et al. [28]:

$$v(x) = \begin{cases} \alpha\omega\left(\frac{|x|-x_0}{\lambda}\right)^2 & \text{when } x_0 \leq |x| \leq x_1 = x_0 + \beta\lambda, \\ 0 & \text{when } |x| < x_0; \end{cases} \tag{9}$$

$\omega$  and  $\lambda$  in  $v(x)$  are angular wave frequency and wavelength, respectively. The two nondimensional parameters  $\alpha$  and  $\beta$  control the strength and the length of the damping zone, respectively.

### 2.1.2. Hydrodynamic Forces Calculation

The hydrodynamic forces on the barge can be obtained by direct integration of the pressure over the instantaneous wetted body surface. The pressure in the fluid can be determined through Bernoulli's equation

$$P = -\rho\left(\frac{\partial\phi}{\partial t} + \frac{1}{2}|\nabla\phi|^2 + gz\right). \tag{10}$$

Thus, the hydrodynamic forces  $\vec{F}$  are expressed as

$$\vec{F} = -\rho \int_{S_b} \left(\frac{\partial\phi}{\partial t} + \frac{1}{2}|\nabla\phi|^2 + gz\right) \vec{n} dl, \tag{11}$$

The time derivative of velocity potential is not explicitly given even when  $\phi$  has been found. An alternative approach is to find  $\partial\phi/\partial t$  by solving a boundary value problem similar to  $\phi$  [29,30].

### 2.2. Numerical Procedures

A 2D boundary element method (BEM) is adopted to solve the IBVP for the velocity potential. BEM is based on Green's second identity

$$A_p\phi_p = \int_{\partial\Gamma} (\ln r_{pq} \frac{\partial\phi_q}{\partial n_q} - \phi_q \frac{\partial \ln r_{pq}}{\partial n_q}) ds, \tag{12}$$

which can reduce the problem by one dimension and consider only the fluid boundaries instead of the fluid domain.  $A_p$  is the solid angle at field point  $p$ ,  $r_{pq}$  is the distance between points  $p$  and  $q$ , and  $\partial\Gamma$  is the boundary of the fluid domain described anticlockwise. This integral representation suggests that the unknown variable  $\phi$  at any point can be determined, if all the values of  $\phi$  and  $\partial\phi/\partial n$  on the boundary are known. We should first discretize the whole fluid boundary into a large number of elements. Then, the velocity potential, its normal derivative, and boundary integral equation can be represented within each element. Finally, we apply the boundary conditions and move all the known terms to the right hand side and the unknown terms to the left to construct the linear matrix equation of the problem [31].

$$\begin{bmatrix} H_{S_N, S_N} & -G_{S_N, S_f} \\ H_{S_f, S_N} & -G_{S_f, S_f} \end{bmatrix} \begin{Bmatrix} (\phi)_{S_N} \\ (\phi_n)_{S_f} \end{Bmatrix} = \begin{bmatrix} G_{S_N, S_N} & -H_{S_N, S_f} \\ G_{S_f, S_N} & -H_{S_f, S_f} \end{bmatrix} \begin{Bmatrix} (\phi_n)_{S_N} \\ (\phi)_{S_f} \end{Bmatrix}. \tag{13}$$

The subscript  $S_N$  indicates that Neumann condition is applied on the corresponding boundaries. The accuracy of the solution of the matrix equation determines the accuracy of the numerical results for a certain mesh.

The BEM solves the IBVP for velocity potential at a given time  $t$  and the time stepping method updates the free surface position and the corresponding velocity potential from time  $t$  to the next time  $t + \Delta t$ . In order to perform the updating, the fluid velocity  $\nabla\phi$  on the free surface must be calculated as well, after  $\phi$  and  $\phi_n$  are obtained. Then the updating is done through time-integration of the kinematic and dynamic free surface boundary conditions in the Lagrangian framework. Here  $\Delta t$  is the time step, which should be set properly to maintain the accuracy of the numerical results. The fluid velocity at the boundary nodes can be determined from  $\phi$  and  $\phi_n$ . Having obtained the fluid velocity at free-surface nodes, a second-order Runge-Kutta time integration method is adopted to update the free-surface position and the velocity potential on it.

For long time simulations, it is often that the free surface nodes may be clustered (too close to each other) or over stretched (too far from each other), which is a source of numerical inaccuracy and possible instability. Special treatments, such as remeshing and smoothing are needed (refer to reference [32] for more details). It should also be mentioned that any remeshing or smoothing treatment would affect the true solution more or less.

### 3. Numerical Results and Discussions

A fifth-order Stokes wave [33] propagating from left to right was employed as the nonlinear regular incident wave. Although the fifth-order incident wave did not satisfy the fully nonlinear free surface condition exactly, it was expected to be a good approximation for the fully nonlinear theory. The incident wave velocity potential  $\phi_I$  and wave elevation  $\eta_I$  are given as follows:

$$\phi_I = \sqrt{\frac{g}{k^3}} \left( \left( \varepsilon - \frac{1}{2} \varepsilon^3 - \frac{37}{24} \varepsilon^5 \right) e^{kz} \sin \theta + \frac{1}{2} \varepsilon^4 e^{2kz} \sin 2\theta + \frac{1}{12} \varepsilon^5 e^{3kz} \sin 3\theta \right), \quad (14)$$

and

$$\eta_I = A \left( \left( 1 - \frac{3}{8} \varepsilon^2 - \frac{211}{192} \varepsilon^4 \right) \cos \theta + \left( \frac{1}{2} \varepsilon + \frac{1}{3} \varepsilon^3 \right) \cos 2\theta + \left( \frac{3}{8} \varepsilon^2 + \frac{99}{128} \varepsilon^4 \right) \cos 3\theta + \frac{1}{3} \varepsilon^3 \cos 4\theta + \frac{125}{384} \varepsilon^4 \cos 5\theta \right), \quad (15)$$

with

$$\theta = kx - \omega_I t, \quad \omega_I = \sqrt{gk} \left( 1 + \frac{1}{2} \varepsilon^2 + \frac{1}{8} \varepsilon^4 \right), \quad (16)$$

and  $\omega_I$  is the incident wave frequency,  $A$  is the incident wave amplitude,  $k = 2\pi/\lambda$  is its wave number.  $\varepsilon = kA$  is often known as the wave steepness.

#### 3.1. Convergence Study and Validation

The convergence study and validation were done through the results of wave diffraction by a single barge. Unfortunately, the authors were not able to find published results of exactly the same parameters as specified previously, i.e., the incident wave as fifth-order Stokes wave and with a rectangular barge. The closest case was found in Koo and Kim [34]. In their study, the main difference is that the incident wave was prescribed as second-order Stokes wave. Another minor difference is that the barge had round corners at the bottom with radius  $R_c$ . Adjustments should be made temporarily in order to compare the results. The case parameters were  $B = 0.5 \text{ m}$  and  $D = 0.25 \text{ m}$ . The water depth of the numerical wave tank was approximately the same order as the incident wavelength. The round corners of the barge had a radius of  $R_c = 0.064 \text{ m}$ . For simplicity, we introduced a dimensionless frequency number  $\xi = \omega_I^2(B/2)/g$ . The incident wave amplitude  $A = 0.035 \text{ m}$ . All simulations were carried out in a fluid domain with the body located at the center and with the truncated boundaries placed at  $x_1 = 5\lambda + B/2$  including  $2\lambda$  damping zone in front of each truncated boundary. The nodes were initially equally distributed on the wetted surface of the body and local zone of the free surface

with element size  $\Delta d$ . Away from the local zone, the element size increased gradually until the far end. Larger elements of equal size were employed on the truncated boundaries and not changed during mesh convergence study, because they were far away from the barge. The nodes on the seabed right below the barge were placed equally with size  $2\Delta d$  throughout all the simulations. During the simulation, the wetted body surface was remeshed every time step, keeping the segment size as  $\Delta d$ . The whole free surface was remeshed and smoothed every five steps. The damping strength was set as 0.2 for all the cases. The damping applied was quite effective in absorbing the outgoing diffracted waves.

The convergence tests with respect to element size and time step were conducted based on the case of  $\xi = 1.0$ , because its frequency lie in the middle of the frequency range. The mesh size only refers to the element on the wetted body surface and the local region of the free surface. Three different meshes and time steps were tested. The convergence tests against element size were studied through comparing results of wave runup histories and hydrodynamic loads on the barge, which are shown in Figures 2 and 3, respectively. The time step was set as  $T/100$  for the calculations.  $T$  is the period of the incident wave. The forces are normalized by  $\rho g A^2/2$ . Unless otherwise specified, the vertical forces given exclude the contribution of initial buoyancy in all the following figures. Large differences, especially phase shifts, were observed between the results of  $\Delta d = \lambda/40$  and  $\Delta d = \lambda/79$  for both the wave runups and the hydrodynamic forces. The results for fine mesh  $\Delta d = \lambda/79$  and finer mesh  $\Delta d = \lambda/157$  were very close but with minor differences. It indicates that finer mesh  $\Delta d = \lambda/157$  could guarantee convergent results. It is therefore the element size used for testing time step.

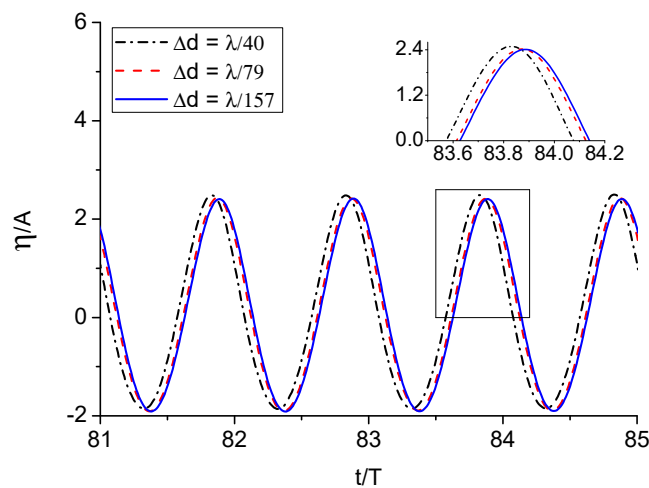


Figure 2. The wave runup histories on the upwave side of the barge for different element size.

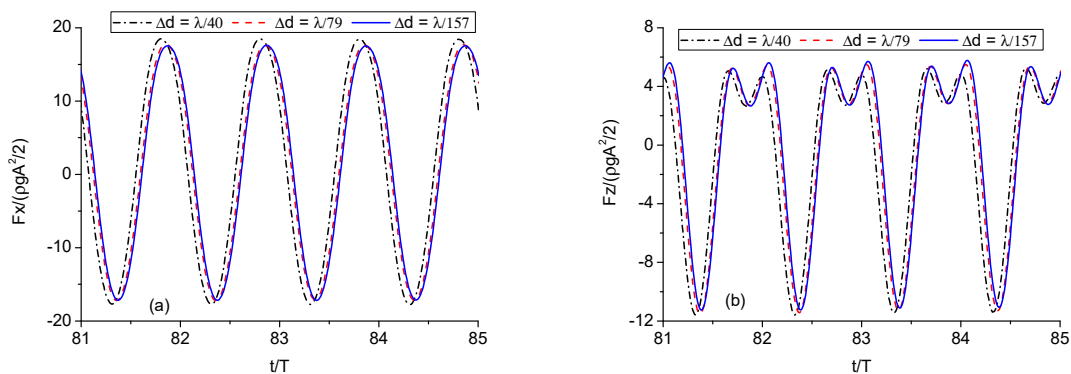


Figure 3. The normalized hydrodynamic force histories on the barge for different element size: (a) Horizontal forces; (b) vertical forces.

We then reran the simulations with  $\Delta t = T/50$  and  $\Delta t = T/200$ , and compared the corresponding wave runups and hydrodynamic forces on the barge in Figures 4 and 5, respectively. We can see that the curves with  $\Delta t = T/100$  and  $\Delta t = T/200$  were virtually coincident with each other, which means that time step  $\Delta t = T/100$  was sufficient to guarantee the temporal convergence. The comparisons between results of different element size and time step suggest that  $\Delta t = T/100$  and  $\Delta d = \lambda/157$  is a better combination for the present problem. The convergence study provides us reference values for choosing the time step and fundamental element size, and proper damping coefficients to obtain convergent results.

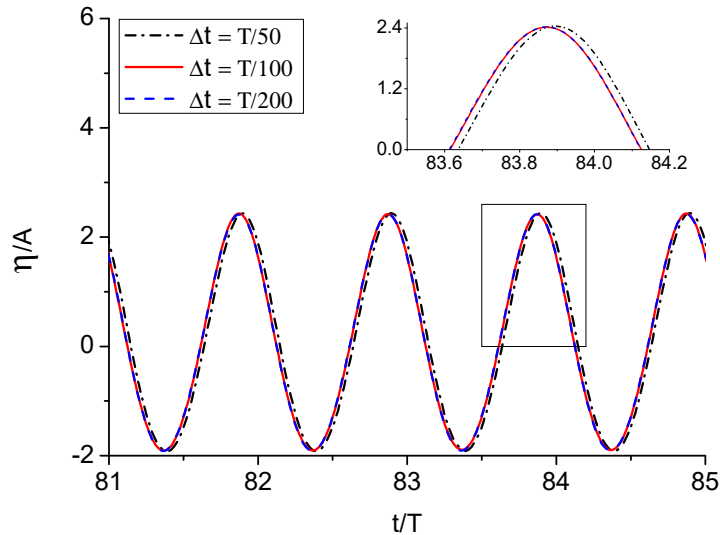


Figure 4. The wave runup histories on the upwave side of the barge for different time step.

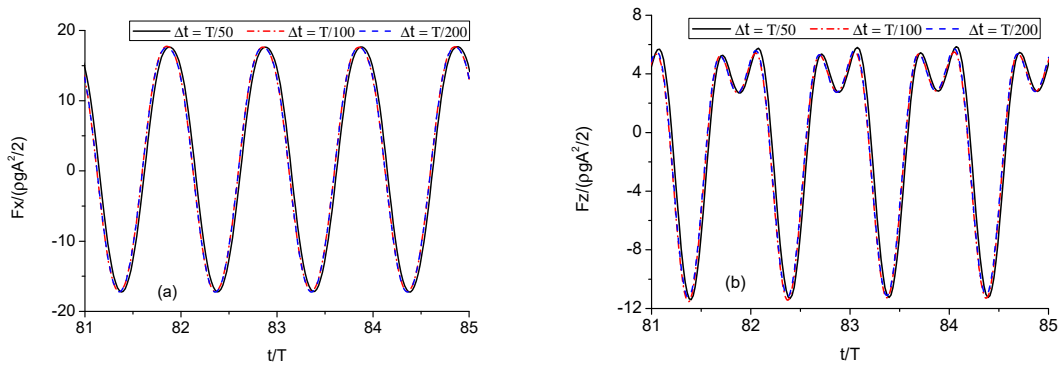


Figure 5. The normalized hydrodynamic force histories on the barge for different time step: (a) Horizontal forces; (b) vertical forces.

To verify the accuracy of the present numerical results, they were compared with published experimental [35], analytical [36], and other numerical results [34,37,38]. The force components were determined through performing Fourier analysis on the steady state part of the force histories. Figure 6 compares the calculated mean drift force  $F_d$  on the barge with other published results. Good agreements were shown in general, especially at the low-frequency range. The present results are generally larger than the results of Koo and Kim. Comparisons of the normalized first harmonic forces  $F^{(1)}$  on the barge are also made in Figure 7 for both horizontal and vertical forces. The calculated first harmonic forces compare well with experimental, analytical, and numerical results. The comparisons indicate that the present numerical code is quite capable of capturing the higher harmonic forces and motions.

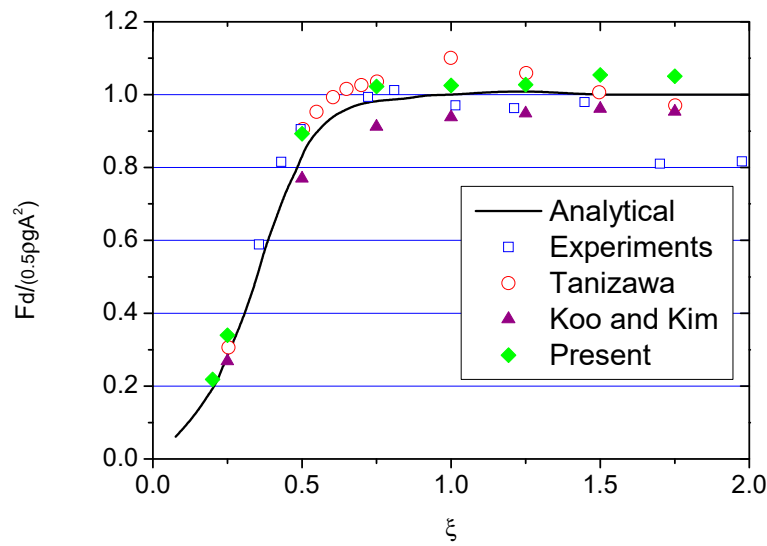


Figure 6. Comparisons of normalized mean drift force on the barge.

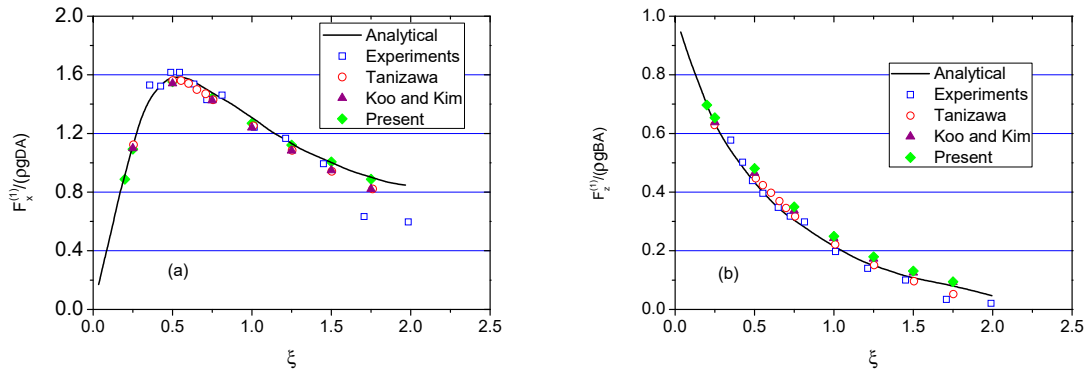


Figure 7. Comparisons of first harmonic forces on the barge: (a) Horizontal force; (b) vertical force.

### 3.2. Pure Wave Diffraction by a Barge

Unless otherwise stated, the results presented later are nondimensionalized, which are based on the length scale  $B$ , gravitational acceleration  $g$  and the density of the fluid  $\rho$ . The barge width is set as  $B = 1\text{ m}$ . The nondimensionalized time  $t'$  and frequency  $\omega'_I$  are respectively expressed as  $t' = t\sqrt{g/B}$  and  $\omega'_I = \omega_I\sqrt{B/g}$  accordingly. For convenience, the prime superscript is dropped. The forces are by nondimensionalized by  $\rho gBD$ . When analyzing the vertical forces, the contribution of static buoyancy is excluded.

The draught of the body was taken as  $D = 1$ . Two sets of simulations associated with incident wave steepness  $\varepsilon = 0.0283$  and  $0.226$  were conducted for a range of frequencies from  $\omega_I = 0.75$  to  $\omega_I = 1.8$ . The hydrodynamic forces on the barge became periodic after a short transient period for all the simulated cases. Examples of the force histories on the structure for lower frequency  $\omega_I = 0.75$  and higher frequency  $\omega_I = 1.8$  are shown in Figures 8 and 9, respectively. The double peaks in the vertical components, especially for high frequency, indicate large higher harmonic forces.

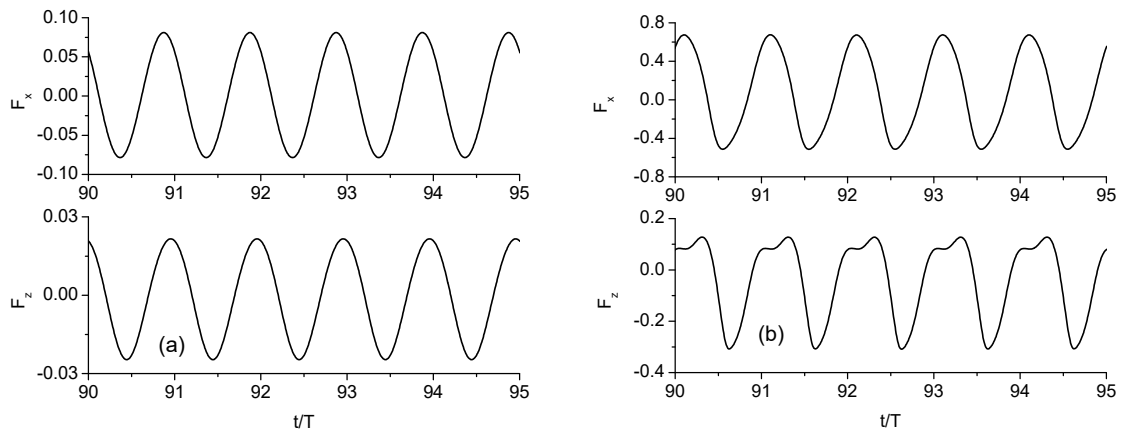


Figure 8. Hydrodynamic forces on the barge when  $\omega_I = 0.75$ : (a)  $\varepsilon = 0.0283$ ; (b)  $\varepsilon = 0.226$ .

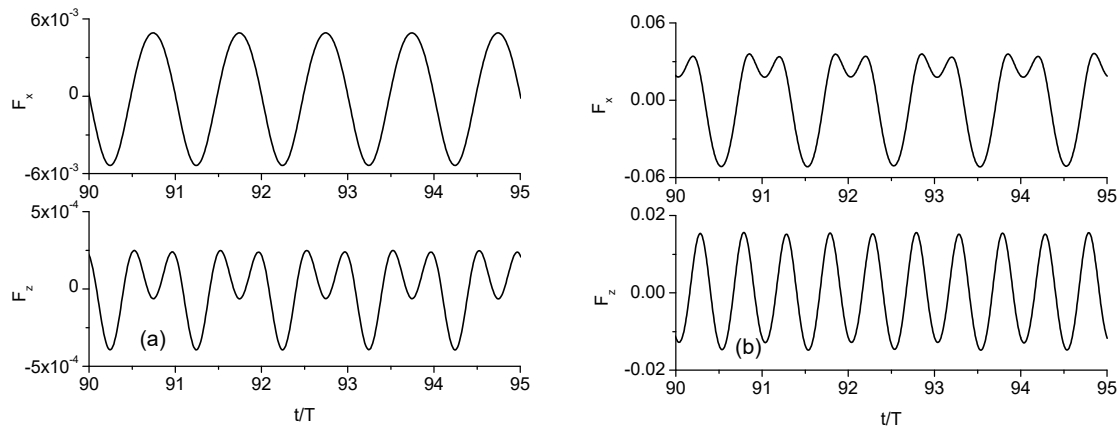


Figure 9. Hydrodynamic forces on the barge when  $\omega_I = 1.8$ : (a)  $\varepsilon = 0.0283$ ; (b)  $\varepsilon = 0.226$ .

In order to distinguish the hydrodynamic force components, Fourier analysis was performed on the steady-state part of the force history. Figure 10 presents the horizontal and vertical force components for  $\varepsilon = 0.226$ . As can be seen, the high-order harmonic forces cannot be neglected as they play an important role. The second harmonic vertical force in particular was actually larger than the first harmonic force after a certain frequency. The higher frequency means shorter waves. This phenomenon is also mentioned and explained in Koo and Kim [34]. They pointed out that this phenomenon is related to a special nonlinear feature of second-order pressure field under standing waves.

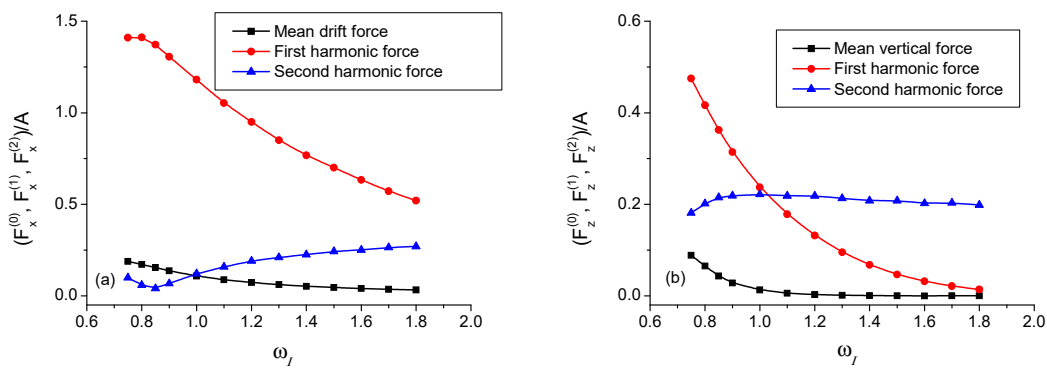


Figure 10. Hydrodynamic force components on the barge when  $\varepsilon = 0.226$ : (a) Horizontal force; (b) vertical force.

### 3.3. Combined Wave Radiation and Diffraction by a Barge

There exist different types of problems such as a body in forced motion and under incoming wave at the same time, especially when the body has sway motion. In such a case, the wave interactions can be strengthened when the body is moving towards the incoming wave or weakened when it is moving away. The effect of the sway motion on wave diffraction will be analyzed in this subsection. The sway motion of the body was sinusoidal, and the amplitude of sway motion was the same as the incident wave amplitude. The draught of the body was set as  $D = 1$ . The incident wave steepness was set as 0.0283 in all the simulations.

#### 3.3.1. Sway Motion with Same Frequency as Incident Wave

The interactions of the diffracted and radiated waves depend on their phase difference. The wave diffraction effect on the body can be changed as a result. The following study will investigate how the sway motion affects the hydrodynamic forces on the body with regard to different wave lengths. The wave length is determined through the dispersion relation.

Long wave diffraction and radiation by sway motion of the body was studied with  $\omega_I = 0.75$ . The corresponding wavelength  $\lambda$  was about 11.18. Figure 11 compares the wave runups on both sides of the body with and without sway motion. They are changed greatly as expected, especially on the leewave side. The body motion not only made the wave runup on the leewave side more than two times higher, but also changed the phase of it by  $78^\circ$ . The wave runup in all the figures is normalized by the amplitude of the incoming wave. The hydrodynamic forces on the body were affected accordingly as shown in Figure 12. The sway motion actually decreased the hydrodynamic horizontal force on the body to a large extent. Specifically, the amplitude of the horizontal force with sway motion is only about a quarter of that of pure diffraction in this case. This is because the horizontal force resulted from the pressure difference between the two sides of the body and the sway motion made the difference smaller as shown in Figure 11. There was also clear phase shift between the horizontal forces. The vertical force, which is associated with the pressure on the bottom of the body, was hardly affected.

The low wave frequency corresponded to long wave length relative to the body dimension, where the wave diffraction effect was of less significance. For intermediate wave with  $\lambda = 7.76$   $\omega_I = 0.9$ , the diffraction and radiation problem was also studied. The comparisons of wave runups and hydrodynamic forces are given in Figures 13 and 14, respectively. Similar conclusions can be drawn as in the long wave case. The sway motion of the body caused clear phase shifts of wave runups on both sides, especially the leewave side. These phase shifts led to phase difference between horizontal forces. The phase shifts between horizontal forces will be studied later. The sway motion makes the horizontal force half of that of pure diffraction in this case.

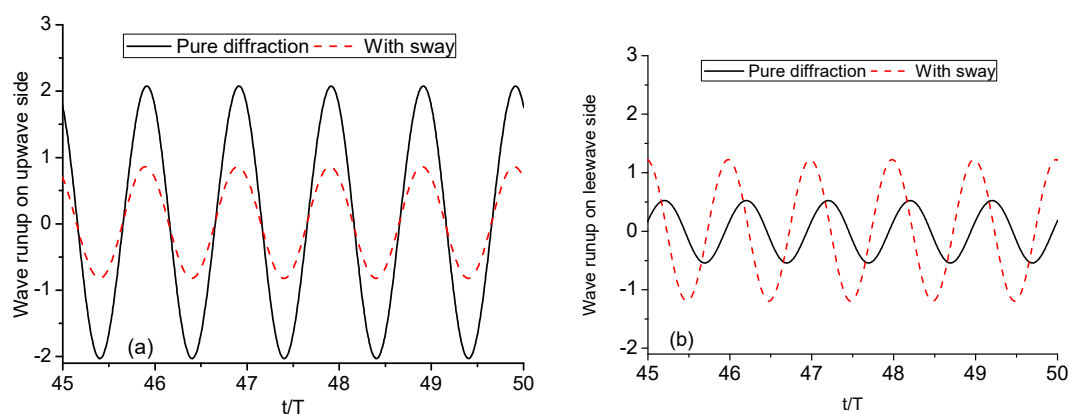


**Figure 11.** The comparison of wave runup on the body when  $\omega_I = 0.75$ : (a) Wave runup on upwave side; (b) wave runup on leewave side.

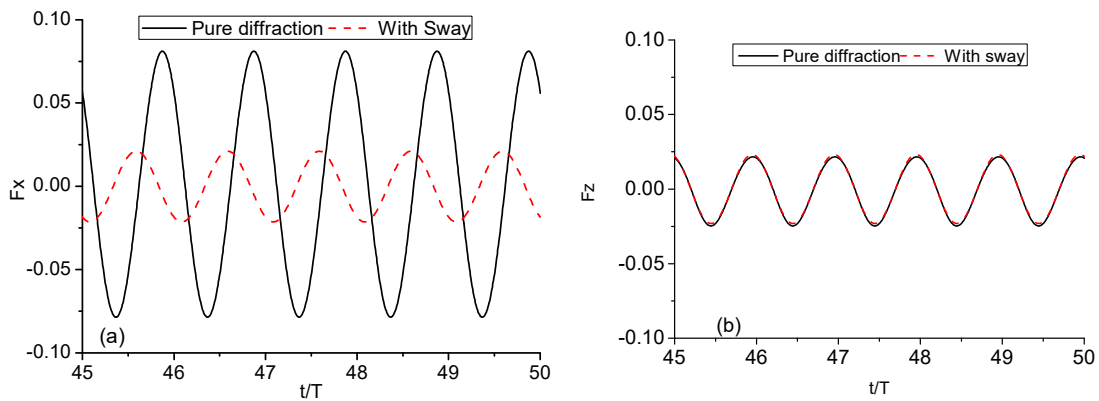


**Figure 12.** The comparison of hydrodynamic forces on the body when  $\omega_I = 0.75$ : (a) Horizontal force; (b) vertical force.

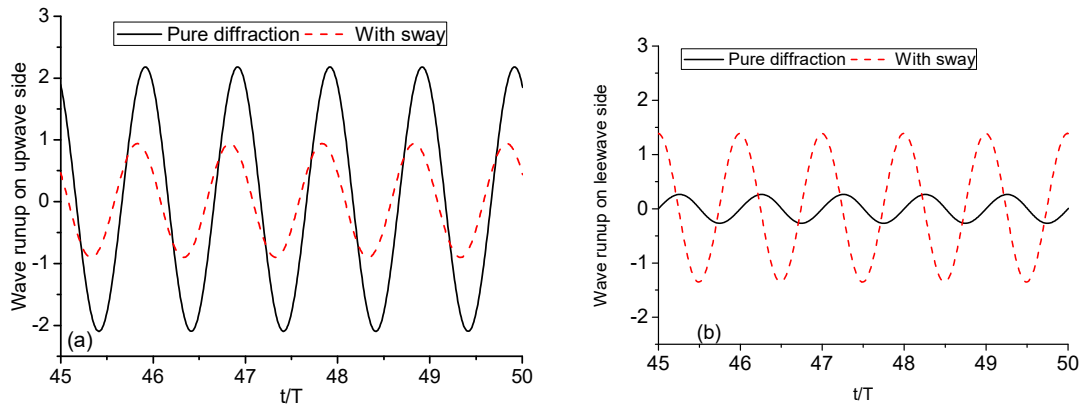


**Figure 13.** The comparison of wave runup on the body when  $\omega_I = 0.9$ : (a) Wave runup on upwave side; (b) wave runup on leewave side.

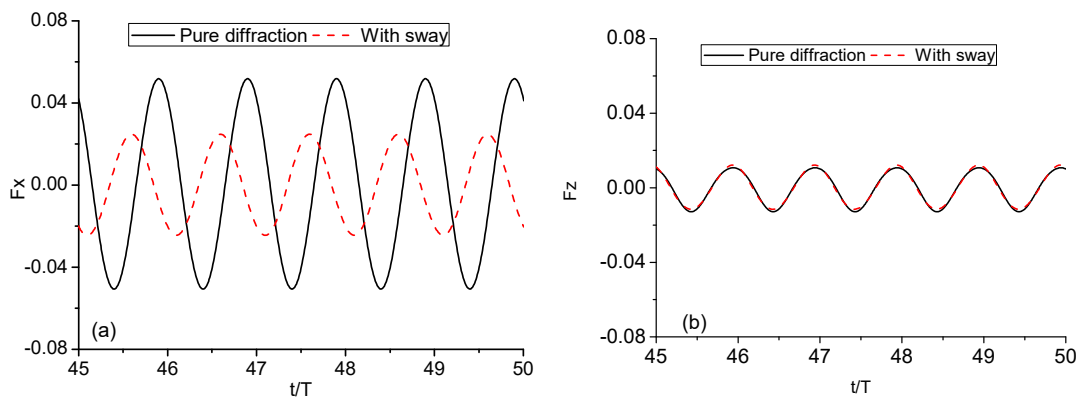


**Figure 14.** The comparison of hydrodynamic forces on the body when  $\omega_I = 0.9$ : (a) Horizontal force; (b) vertical force.

To test the effect of sway motion on short wave diffraction when the diffraction force is of significance, we considered the case of  $\omega_I = 1.8$ ,  $\lambda = 2$ . The comparison of wave runup on the body is presented in Figure 15. When there was no body motion present, standing wave trains were formed in front of the body and nearly no wave behind. The superposition of the incident wave, diffracted wave, and the wave generated by sway motion made the wave runups on both sides of the body much larger. Meanwhile, the hydrodynamic load on the body was enlarged, as shown in Figure 16. It is

worth mentioning that in this case, the second harmonic vertical force was even larger than the first harmonic force, which is known from its spectral analysis in Figure 17. Furthermore, the sway motion did not change its first harmonic component, but increased its second harmonic force considerably. This can be explained by the argument in Wu [39]. The periodic sway motion itself will lead to vertical force with components of frequencies  $2n\omega_I, n = 0, 1, 2, \dots$ . Thus, it can significantly enlarge the steady and double frequency vertical force components.

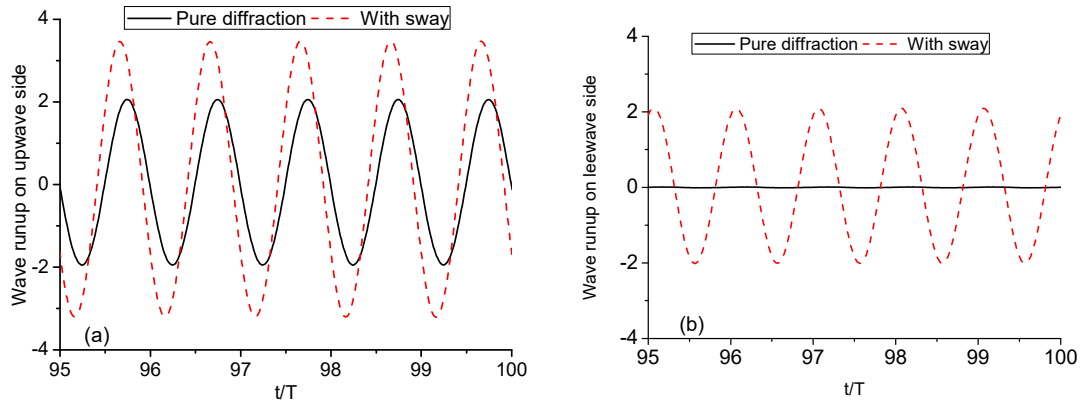


**Figure 15.** The comparison of wave runup on the body when  $\omega_I = 1.8$ : (a) Wave runup on upwave side; (b) wave runup on leewave side.

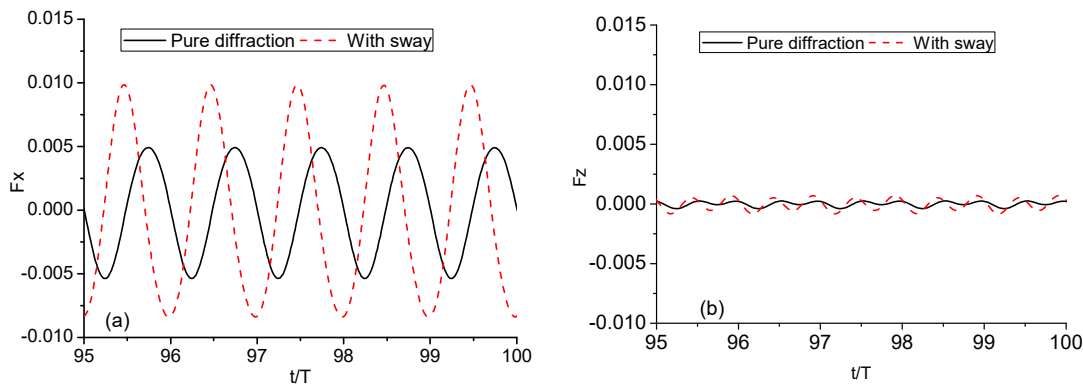


**Figure 16.** The comparison of hydrodynamic forces on the body when  $\omega_I = 1.8$ : (a) Horizontal force; (b) vertical force.

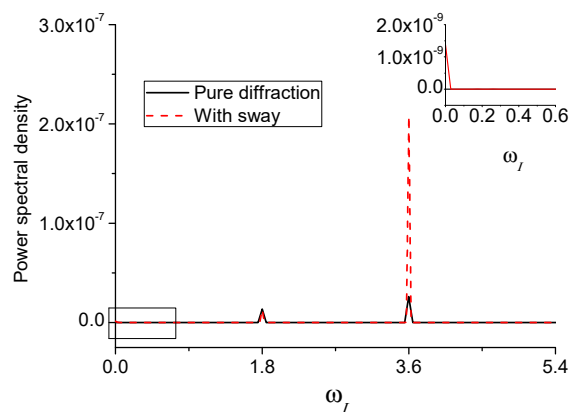


**Figure 17.** Power spectral analysis of vertical forces when  $\omega_I = 1.8$ .

Particularly, the sheltering effect behind the body, which is related to diffraction problem, was weakened by waves generated by sway motion. In terms of hydrodynamic forces, the horizontal force can be either enlarged or reduced with phase shift. From the above three cases, we notice that the change of horizontal force actually depended on the incident wave frequency. To get a better idea of how they are related, a series of cases with frequencies ranging from  $\omega_I = 0.75$  to  $\omega_I = 1.8$  were simulated. The amplitudes of horizontal forces associated with both pure diffraction and with sway motion cases were then calculated and compared. Using the horizontal forces of pure diffraction case as reference, the relative change of their amplitudes is given in Figure 18. The relative change is presented against both wave frequency and wave length. Generally speaking, sway motion with low frequency reduced the overall horizontal force. The reducing effect decreased as the frequency increased until a critical frequency was reached where the amplitudes of horizontal forces for pure diffraction and with sway were equal. The critical frequency was about  $\omega_I = 1.25$ . After that, the higher the frequency, the bigger the horizontal force increasing effect. As for the wave length, the relative change tendency was opposite to that against wave frequency.

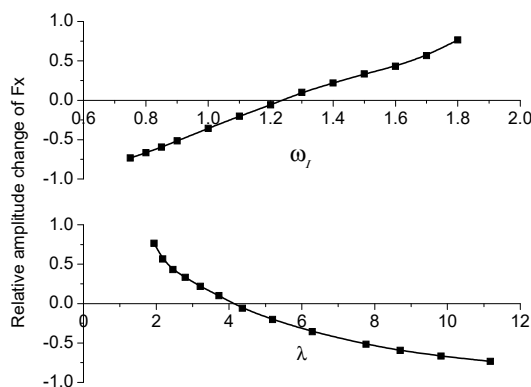


Figure 18. The relative change of horizontal force due to sway motion against wave frequency and wave length.

As mentioned earlier, sway motion of the body can cause noticeable phase shifts of horizontal forces. The magnitudes of the shifts depend on the incident wave frequency, or rather the incident wave length. Figure 19 gives the phase shifts against wave frequency and their dependency on wave length. The phase shift exceeded  $\pi/2$  in all the simulated cases. It reached its maximum value at  $\omega_I = 0.9$  or  $\lambda = 7.76$ .

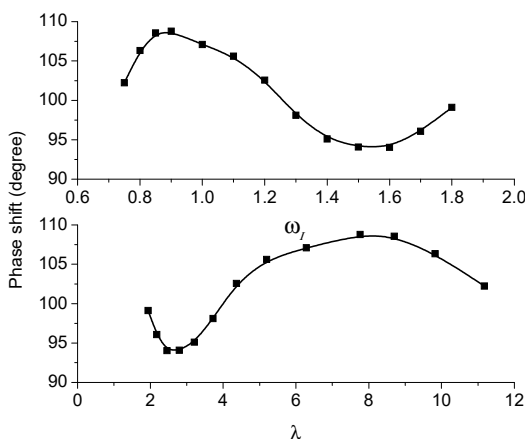
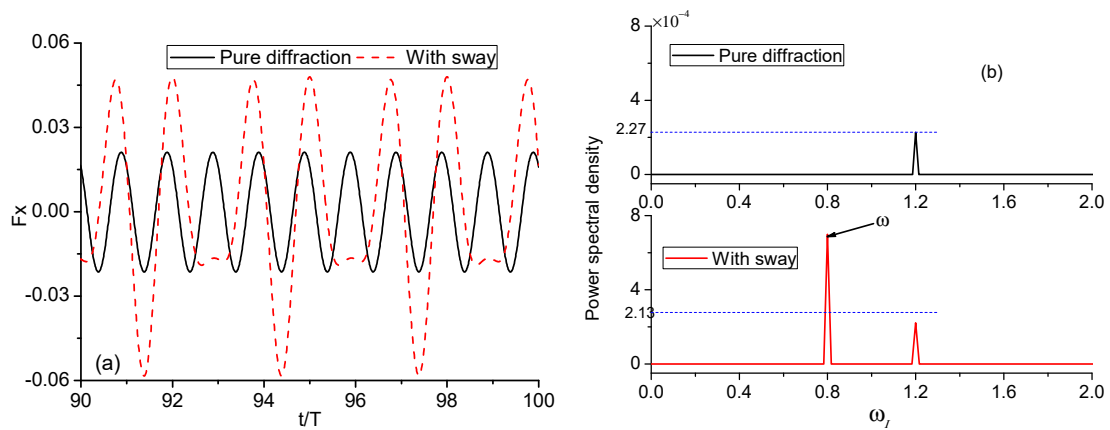


Figure 19. Phase shifts of horizontal forces against wave frequency and wave length.

### 3.3.2. Sway Motion with Different Frequency from Incident Wave

The incident wave frequency was set as  $\omega_I = 1.2$ , partly because this frequency lies in the middle of the frequency range and partly because it is close to the critical frequency mentioned above. Next, we ran simulations of forced sway motion with frequency either higher or lower than the incident wave frequency. The frequency of sway motion is denoted as  $\omega$ , and the period  $T$  corresponds to the frequency of sway motion or incident wave, whichever is higher.

The cases with frequencies of sway motion lower than that of incident wave were first studied. Take  $\omega = 0.8$  for instance, and the comparison of their horizontal force histories is shown in Figure 20a. Clearly, the horizontal force with sway motion present had multiple frequencies. Therefore, the spectral analysis of them was performed and is compared in Figure 20b. Two distinct frequencies, of which one relates to sway motion and the other relates to incident wave, were extracted. Moreover, the amplitude of horizontal force associated with sway motion was in fact larger than that of incident wave, which was hardly affected by the sway motion when comparing it to pure diffraction case. One may argue that there should be sum and difference frequency terms in the force as well. As a matter of fact, these terms were too small to show any significance, which can be seen in the close-up figure of spectral analysis Figure 21.



**Figure 20.** The horizontal force histories and their corresponding spectral analysis when  $\omega = 0.8$ : (a) Horizontal force histories; (b) spectral analysis of horizontal force.

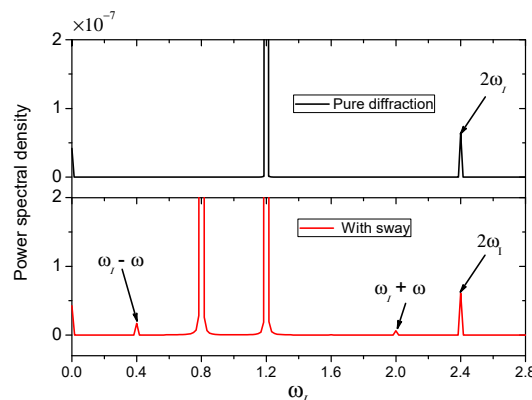


**Figure 21.** Close-up of spectral analysis of horizontal force when  $\omega = 0.8$ .

The frequency  $\omega = 0.8$  was much lower than the incident wave frequency. We now consider the case where  $\omega$  is close to  $\omega_I = 1.2$ . Periodic envelope appeared on the horizontal force history as shown in Figure 22a when  $\omega = 1.1$ . The period of the envelope depended on the difference between  $\omega$  and  $\omega_I$ . The spectral analysis of the horizontal force was conducted and is provided in Figure 22b.

The same conclusion can be drawn as in the previous case. For the cases when  $\omega$  was higher than the incident wave frequency, the pattern of horizontal force on the body was quite different from that when  $\omega$  was lower than  $\omega_I$ . Figure 23a shows the comparison of horizontal force histories of pure diffraction case and the case with sway motion  $\omega = 1.3$ . It can be seen that the sway motion made the horizontal force on the body two times larger. The spectral analysis of them is given in Figure 23b. It is interesting to see that only one single frequency associated with the sway motion existed, while the one with incident wave disappeared. More cases with  $\omega > \omega_I$  were then run to see the horizontal force spectral distribution in case the one with  $\omega = 1.3$  was special. Figure 24 gives the spectral analysis of horizontal force histories. It was confirmed that the frequency related to incident wave disappeared on the horizontal force spectra when  $\omega > \omega_I$ .

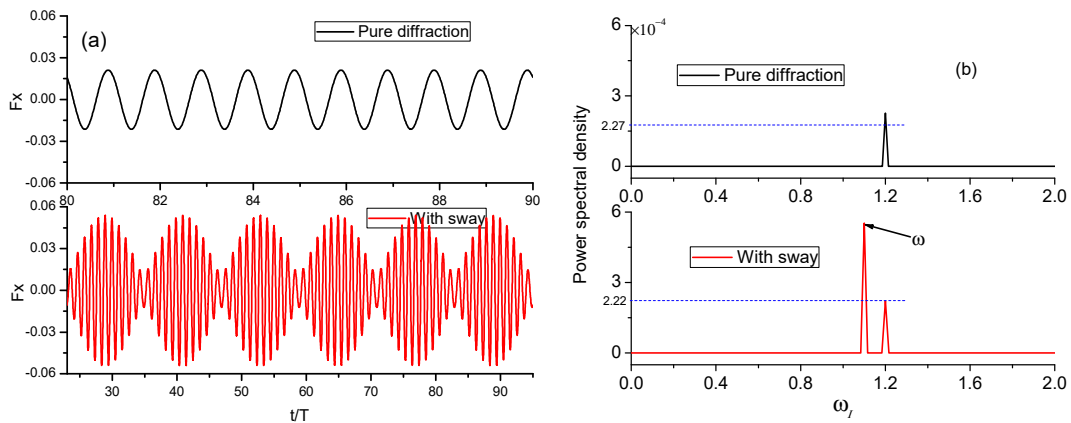


**Figure 22.** The horizontal force histories and their corresponding spectral analysis when  $\omega = 1.1$ : (a) Horizontal force histories; (b) spectral analysis of horizontal force.

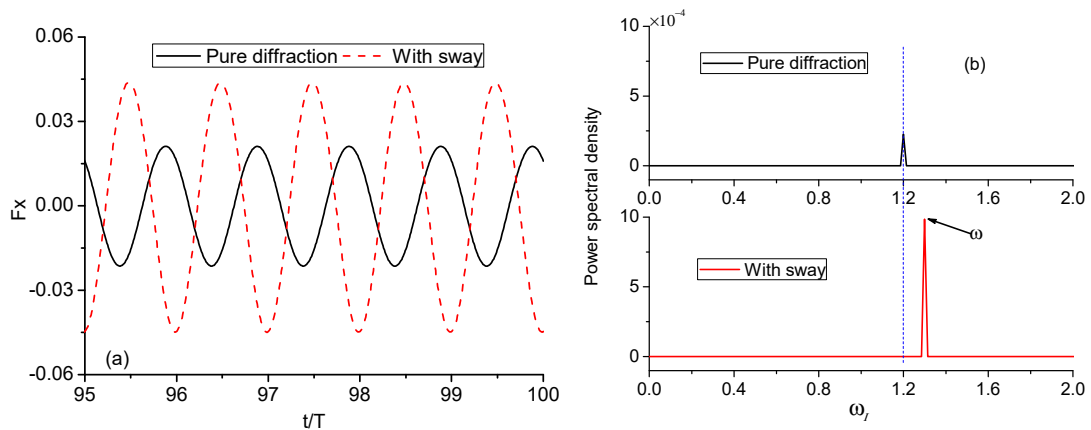


**Figure 23.** The horizontal force histories and their corresponding spectral analysis when  $\omega = 1.3$ : (a) Horizontal force histories; (b) spectral analysis of horizontal force.

In terms of the magnitude of the horizontal force, slower sway motion of the body will always make the resultant force larger. That is because, on one hand, the effect of incident wave was hardly affected by sway motion, and on the other hand, the horizontal force itself resulting from the sway motion was bigger. It can be shown in Figure 25, which gives the power spectral analysis of horizontal force histories with slower sway motion. When the frequency of sway motion was higher, there was no clear pattern.

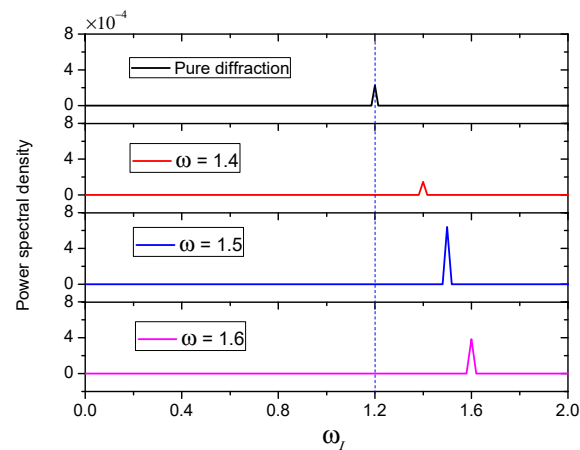


**Figure 24.** Spectral analysis of horizontal force histories with high frequencies of sway motion.

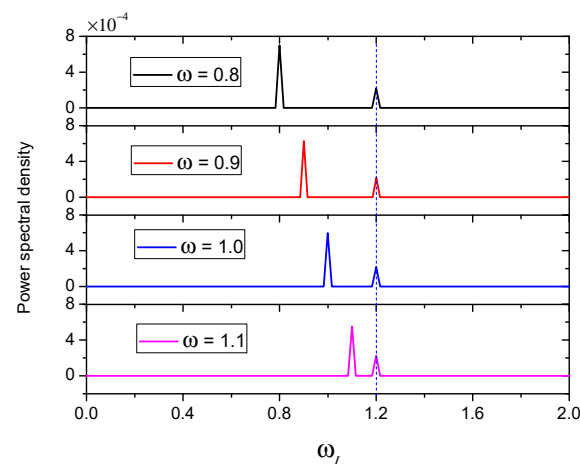


**Figure 25.** Spectral analysis of horizontal force histories with slower sway motion.

#### 4. Conclusions

This paper studies the combined wave radiation and diffraction by a single barge through fully nonlinear numerical simulations in the time domain. The associated initial boundary value problem for the velocity potential is solved using boundary element method together with a time stepping scheme. In order to keep the simulations running for a sufficiently long time, some special numerical treatments are also applied to the free surface, such as remeshing, smoothing, jet, and thin spray cutting. The findings in this paper are all based on the results obtained from potential flow theory.

In the cases for a single body under incident wave and with forced sway motion, the amplitude of sway motion is always kept the same as the incident wave amplitude and with a  $\pi/2$  initial phase difference. Some of the interesting findings by spectral analysis of the hydrodynamic forces are:

- (1) When the frequencies are also the same, sway motion will reduce the overall horizontal force when the frequency is lower than a critical frequency  $\omega = 1.2$ . After that, the higher the frequency, the bigger the horizontal force increasing effect.
- (2) When the frequencies are different, the incident wave frequency  $\omega_I$  is set as the critical frequency  $\omega_I = 1.2$ . It has been found that for horizontal forces, only the frequency associated with sway motion  $\omega$  is visible, while the one with incident wave frequency nearly disappears when  $\omega > 1.2$ .
- (3) In terms of the magnitude of the horizontal force, sway motion of the body will always make the resultant force larger than that of pure diffraction case when  $\omega < 1.2$  within the simulated frequency range.

The above phenomena are expected to be valid in other configurations, such as a single body with different draught, even though the critical frequency may be different. It is worth mentioning that the interactions of diffracted and radiated waves also depend on the relative phase between the incident wave and forced sway motion. The effects of phase difference between them are not considered in this paper. The above conclusions are drawn based on the difference of  $\pi/2$ .

**Author Contributions:** Y.L. developed models, analyzed data, and wrote the manuscript. B.X. designed the study, reviewed results, and edited the manuscript. D.Z. reviewed results and edited the manuscript. X.S. reviewed results and edited the figure. W.Z. reviewed results and edited the manuscript. All authors have read and agreed to the published version of the manuscript.

**Funding:** This research was funded by Senior Talent Foundation of Jiangsu University (grant number 18JDG036 and 18JDG034). Open Research Subject of Key Laboratory (Fluid Machinery and Engineering Research Base) of Sichuan Province (grant number szjj2019-028), Jiangsu Planned Projects for Postdoctoral Research Funds (Grant number 2018K102C), National Natural Science Foundation of China (Grant number 51776087, 51579118), National Key Research and Development Program of China (Grant number 2017YFC0404201), 333 Project of Jiangsu Province (Grant number 2016III-2731), Six Talent Peaks Project in Jiangsu Province (Grant number HYG-008) and Qing Lan Project.

**Acknowledgments:** The authors appreciate Jiangsu University, key laboratory (Fluid Machinery and Engineering Research Base) of Sichuan province and Jiangsu province for their funding and support. Special thanks go to G.X. Wu from University College London for his helpful suggestions and discussions on this work.

**Conflicts of Interest:** The authors declare no conflict of interest.

## References

1. Longuet-Higgins, M.S.; Cokelet, E.D. The deformation of steep surface waves on water I. A numerical method of computation. *Proc. R. Soc. Lond. A Math. Phys. Sci.* **1976**, *350*, 1–26. [[CrossRef](#)]
2. Ursell, F. On the heaving motion of a circular cylinder on the surface of a fluid. *Q. J. Mech. Appl. Math.* **1949**, *2*, 218–231. [[CrossRef](#)]
3. Kim, W.D. On the harmonic oscillations of a rigid body on a free surface. *J. Fluid Mech.* **1965**, *21*, 427–451. [[CrossRef](#)]
4. Black, J.L.; Mei, C.C.; Bray, M.C.G. Radiation and scattering of water waves by rigid bodies. *J. Fluid Mech.* **1971**, *46*, 151–164. [[CrossRef](#)]
5. Lee, J.F. On the heave radiation of a rectangular structure. *Ocean Eng.* **1995**, *22*, 19–34. [[CrossRef](#)]
6. Wu, G.X.; Taylor, R.E. Time stepping solutions of the two-dimensional nonlinear wave radiation problem. *Ocean Eng.* **1995**, *22*, 785–798. [[CrossRef](#)]
7. Maiti, S.; Sen, D. Nonlinear heave radiation forces on two-dimensional single and twin hulls. *Ocean Eng.* **2001**, *28*, 1031–1052. [[CrossRef](#)]
8. Hu, P.; Wu, G.X.; Ma, Q.W. Numerical simulation of nonlinear wave radiation by a moving vertical cylinder. *Ocean Eng.* **2002**, *29*, 1733–1750. [[CrossRef](#)]
9. Wang, C.Z.; Wu, G.X.; Drake, K.R. Interactions between nonlinear water waves and non-wall-sided 3D structures. *Ocean Eng.* **2007**, *34*, 1182–1196. [[CrossRef](#)]
10. Havelock, T.H. The pressure of water waves upon a fixed obstacle. *Proc. R. Soc. Lond. Ser. A Math. Phys. Sci.* **1940**, *175*, 409–421. [[CrossRef](#)]
11. Molin, B. Second-order diffraction loads upon three-dimensional bodies. *Appl. Ocean Res.* **1979**, *1*, 197–202. [[CrossRef](#)]
12. Kim, M.H.; Yue, D.K.P. The complete second-order diffraction solution for an axisymmetric body Part 1. Monochromatic incident waves. *J. Fluid Mech.* **1989**, *200*, 235–264. [[CrossRef](#)]
13. Sclavounos, P.D. Radiation and diffraction of second-order surface waves by floating bodies. *J. Fluid Mech.* **1988**, *196*, 65–91. [[CrossRef](#)]
14. Wu, G.X.; Taylor, R.E. The second order diffraction force on a horizontal cylinder in finite water depth. *Appl. Ocean Res.* **1990**, *12*, 106–111. [[CrossRef](#)]
15. Liu, Y.; Xue, M.; Yue, D.K.P. Computations of fully nonlinear three-dimensional wave-wave and wave-body interactions. Part 2. Nonlinear waves and forces on a body. *J. Fluid Mech.* **2001**, *438*, 41–66. [[CrossRef](#)]
16. Faltinsen, O.M.; Newman, J.N.; Vinje, T. Nonlinear wave loads on a slender vertical cylinder. *J. Fluid Mech.* **1995**, *289*, 179–198. [[CrossRef](#)]

17. Malenica, Š.; Molin, B. Third-Harmonic wave diffraction by a vertical cylinder. *J. Fluid Mech.* **1995**, *302*, 203–229. [[CrossRef](#)]
18. Ma, Q.W.; Wu, G.X.; Taylor, R.E. Finite element simulations of fully non-linear interaction between vertical cylinders and steep waves. Part 2: Numerical results and validation. *Int. J. Numer. Methods Fluids* **2001**, *36*, 287–308. [[CrossRef](#)]
19. Bai, W.; Taylor, R.E. Numerical simulation of fully nonlinear regular and focused wave diffraction around a vertical cylinder using domain decomposition. *Appl. Ocean Res.* **2007**, *29*, 55–71. [[CrossRef](#)]
20. Bai, W.; Taylor, R.E. Fully nonlinear simulation of wave interaction with fixed and floating flared structures. *Ocean Eng.* **2009**, *36*, 223–236. [[CrossRef](#)]
21. Ogilvie, T.F. Second-order hydrodynamic effects on ocean platforms. In *International Work Shop on Ship and Platform Motions*; University of California: Berkeley, CA, USA, 1983; pp. 205–265.
22. Cao, Y.; Beck, R.F.; Schultz, W.W. Nonlinear computation of wave loads and motions of floating bodies in incident waves. In *Proceedings of the 9th International Workshop on Water Waves and Floating Bodies*, Kuju Fukuoka, Japan, 17–20 April 1994; pp. 33–37.
23. Kashiwagi, M. Non-linear simulations of wave-induced motions of a floating body by means of the mixed Eulerian-Lagrangian method. *Proc. Inst. Mech. Eng. Part C J. Mech. Eng.* **2000**, *214*, 841–855. [[CrossRef](#)]
24. Koo, W.; Kim, M.H. Freely floating-body simulation by a 2D fully nonlinear numerical wave tank. *Ocean Eng.* **2004**, *31*, 2011–2046. [[CrossRef](#)]
25. Yan, S.; Ma, Q.W. Numerical simulation of fully nonlinear interaction between steep waves and 2D floating bodies using the QALE-FEM method. *J. Comput. Phys.* **2007**, *221*, 666–692. [[CrossRef](#)]
26. Zhou, B.Z.; Wu, G.X. Resonance of a tension leg platform excited by third-harmonic force in nonlinear regular waves. *Philos. Trans. R. Soc. A Math. Phys. Eng. Sci.* **2015**, *373*, 20140105. [[CrossRef](#)]
27. Li, Y. Fully nonlinear analysis of second-order gap resonance between two floating barges. *Eng. Anal. Bound. Elem.* **2019**, *106*, 1–19. [[CrossRef](#)]
28. Cointe, R.; Geyer, P.; King, B.; Molin, B. Nonlinear and linear motions of a rectangular barge in a perfect fluid. In *Proceedings of the 18th Symposium on Naval Hydrodynamics*, Ann Arbor, MI, USA, 19–24 August 1990.
29. Wu, G.X.; Taylor, R.E. The coupled finite element and boundary element analysis of nonlinear interactions between waves and bodies. *Ocean Eng.* **2003**, *30*, 387–400. [[CrossRef](#)]
30. Li, Y.; Zhang, C. Analysis of wave resonance in gap between two heaving barges. *Ocean Eng.* **2016**, *117*, 210–220. [[CrossRef](#)]
31. Sun, S.Y.; Sun, S.L.; Wu, G.X. Oblique water entry of a wedge into waves with gravity effect. *J. Fluids Struct.* **2015**, *52*, 49–64. [[CrossRef](#)]
32. Li, Y. Fully Nonlinear Numerical Simulations of Wave Interactions with Multiple Structures at Resonance. Ph.D. Thesis, University College London, London, UK, 2017.
33. Fenton, J.D. A fifth-order Stokes theory for steady waves. *J. Waterw. Port Coast. Ocean Eng.* **1985**, *111*, 216–234. [[CrossRef](#)]
34. Koo, W.C.; Kim, M.H. Fully nonlinear wave-body interactions with surface-piercing bodies. *Ocean Eng.* **2007**, *34*, 1000–1012. [[CrossRef](#)]
35. Nojiri, N.; Murayama, K. A study on the drift force on twodimensional floating body in regular waves. *Trans. West Jpn. Soc. Nav. Archit.* **1975**, *51*, 131–152.
36. Maruo, H. On the Increase of the Resistance of a Ship in Rough Seas. *J. Zosen Kiokai* **1960**, *1960*, 5–13. [[CrossRef](#)]
37. Tanizawa, K.; Minami, M. On the accuracy of NWT for radiation and diffraction problem. Abstract for the 6th Symposium on Nonlinear and Free-Surface Flow. 1998.
38. Li, X.J.; Chen, B.; Luo, X.W.; Zhu, Z.C. Effects of flow pattern on hydraulic performance and energy conversion characterisation in a centrifugal pump. *Renew. Energy* **2019**, in press. [[CrossRef](#)]
39. Wu, G.X. A note on non-linear hydrodynamic force on a floating body. *Appl. Ocean Res.* **2000**, *22*, 315–316. [[CrossRef](#)]

